# An Integrated Solar Cell with Built-in Energy Storage Capability

Husain Almakrami, Zi Wei, Guanzhou Lin, Xinfang Jin, Ertan Agar, and Fuqiang Liu\*

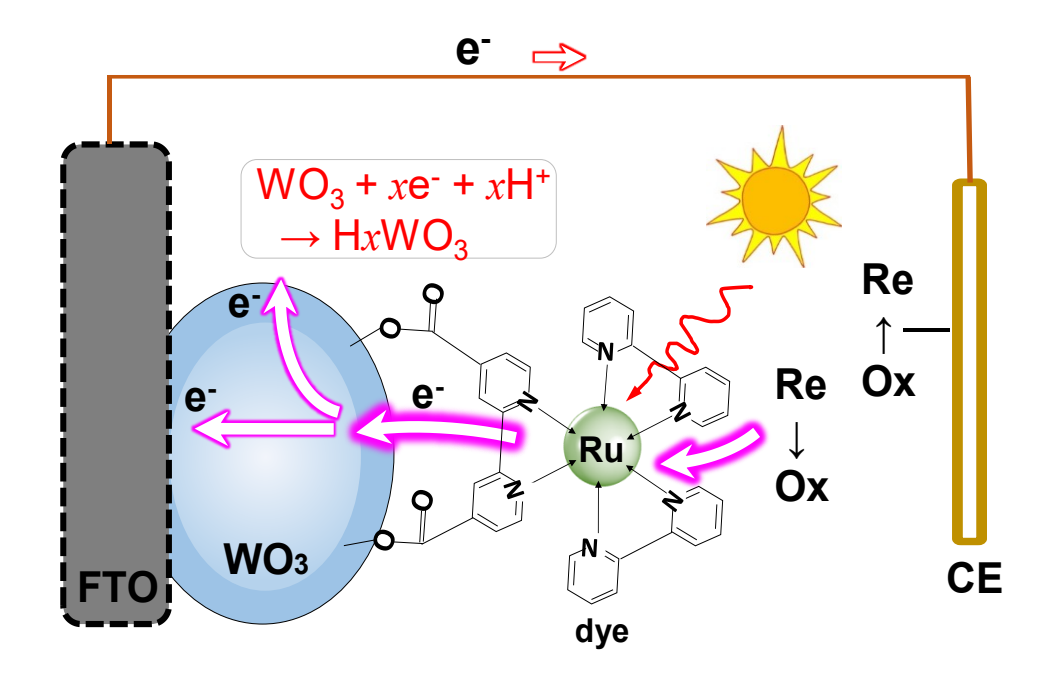
Department of Mechanical Engineering, University of Massachusetts Lowell Lowell, MA 01854

<sup>\*</sup> E-mail: Fuqiang liu@uml.edu, Tel: 1-978-934-2927, Fax: 1-978-934-3048

### **ABSTRACT**

Due to inherent intermittency nature of light, energy must be stored within external batteries in photovoltaic systems, resulting in systems that are fragile and expensive. Internal storage integration can offer highly robust systems at substantially low cost if external batteries are replaced by internal ones. Despite excellent photovoltaic power conversion efficiencies displayed by titanium dioxide (TiO<sub>2</sub>) mesoporous nanoparticle structures in Dye-sensitized solar cells, they are short of storage capability. Alternatively, photochromic Tungsten Oxide (WO<sub>3</sub>) nanoparticle films are investigated as potential candidates for the photoanode in our solar storage cell. In this work, we demonstrate an integrated solar storage cell that can potentially deliver solar power even in darkness owing to its integrated energy storage capability. The cell is built upon the dyesensitized solar cell platform using a photochromic WO<sub>3</sub> electrode and has the ability to simultaneously generate and store charges during the day and discharge the stored charges during night. Specifically, three different batches of WO<sub>3</sub> nanoparticles, each of unique particle size, are investigated in terms of their compatibility with the solar storage cell and built-in storage capacity. Our results revealed that the solar storage cell with the largest WO<sub>3</sub> particle size (~100 nm) exhibits the best transient voltage-current characteristics. On the other hand, intermediate WO<sub>3</sub> particle size (60-95 nm) displayed the best storage capacity when undergoing a prolonged photocharging. These comparative investigations shed light on the morphological difference in electrode, active surface area, porosity-dependent electron transport, and redox diffusion coefficient that have a significant impact on the photo/electrochemical properties of the electrodes.

**Keywords:** Solar energy, photoelectrochemical, vanadium redox, dye-sensitized solar cell, storage



#### 1. INTRODUCTION

While solar power with its rising market penetration is transforming how electricity is produced and utilized, there is a remarkable growing demand for solar-storage devices with improved power quality and reliability to circumvent the inherent intermittency of solar energy. Current practices to enable solar-storage systems normally rely on rechargeable batteries that are externally coupled with PV systems [1], in which solar energy is first converted to electricity and then stored in the form of chemical energy. However, this typically results in redundancy of resources and missed opportunities to increase performance through synergistic integration, making these systems expensive and inefficient. Instead, internal integration of storage capability into solar cells that allows for direct conversion of solar energy into chemical energy without the unnecessary intermediate step (i.e., electricity) at the point of energy generation is more attractive for higher efficiency and reliability.

Most of the systems reported in developing a solar storage cell (SSC) with internal storage capability are a simple addition of two devices: a solar cell and a capacitor or battery with multiple components. However, the fabrication of a multicomponent device and control of electric current switching between photocharging and discharging modes are complicated. For example, a high solar-to-electricity conversion efficiency (11.3%) was demonstrated using a cell consisting of a Cd(Se,Te)/S<sub>x</sub> and Sn/SnS storage system, resulting in a solar cell with a continuous output [2]. To accommodate this, smart load switch controllers have to be employed in the cell module to manually allow photocharge and discharge under different conditions.

Automatic switching between photocharge and discharge (i.e., switch-free) in a SSC would be highly desirable to not only create a compact system, but also shorten system-level response time to external light condition change. A high-capacity photochromic WO<sub>3</sub> electrode in a

photoelectrochemical (PEC) storage cell [3-10], as demonstrated by Liu et al [4], could offer a unique opportunity to realize switch-free solar energy storage. In this work, we explored an SSC using dye-sensitized WO<sub>3</sub> electrodes in a PEC cell and investigated the built-in storage capacity using vanadium redox species. Vanadium redox species have been employed in an all-vanadium solar storage cell, which has been demonstrated to achieve a maximum solar conversion efficiency that is over four times of that of photolysis of water even using pristine TiO<sub>2</sub> [11, 12] due to the fast PEC reaction kinetics of the redox species [11]. The cell has been shown to achieve a high Faradaic efficiency of 95% [3] and peak incident-photon-to-current efficiency (IPCE) of 45% in solar energy storage [13]. In addition, nanostructured TiO<sub>2</sub> photocatalysts [14], dye sensitization [15], alternative supporting electrolyte that has significantly prolonged electron lifetime by 41x [13], and forced convective flow of electrolytes [16] have been demonstrated to enhance the photocurrent and greatly extend the state-of-charge during solar energy storage. Recently, a reversible electron-storage process under alternate light and dark conditions was discovered in a photochromic material (e.g., WO<sub>3</sub>) [4, 17, 18], which, upon removal of light, automatically releases the stored electrons forming the dark-condition discharge current.

Dye-sensitized solar cells (DSSCs) have been deemed as a favorable alternative to conventional photovoltaic devices in a wide range of applications [19-21]. Though much of the research focused on either boosting DSSC efficiency [22-24] or developing different sensitizing materials [25-27], only a handful of studies have been devoted to realizing storage potential in DSSCs. Energy storage can be realized by the combination of DSSCs and capacitors based on active carbon [28], carbon nanotubes [29], conductive polymer [30], PVDF/ZnO nanocomposite [31], and RuO<sub>2</sub> [32]. These systems, primarily based on tri-iodide/iodide redox couple, could only offer a limited energy density and a short self-discharge time of no more than a few minutes.

To increase the discharge duration, in this work the proposed SSC takes advantages of the known photochromic property of WO<sub>3</sub> in conjunction with vanadium redox species. Though photoanodes using WO<sub>3</sub>/TiO<sub>2</sub> in DSSCs have been already studied, they are primarily employed to improve electron transfer and suppress charge recombination, not much to enable energy storage capability [19, 33]. Besides, the studied DSSC systems are primarily limited to iodine-based electrolytes. Herein we aim to take advantage of the important synergy between electron storage of WO<sub>3</sub> and the highly-active vanadium electrolyte [4, 13, 18]. In this work, the implication of both WO<sub>3</sub> participle size and electrode porosity to electron transfer rate, redox diffusion coefficient, and therefore electron storage capacity was studied, and prolonged dark-condition discharge has been demonstrated. Therefore, the developed SSC potentially could potentially offer a unique strategy to resolve the inherent intermittency of solar energy.

## 2. Working Principle

The storage capability of the SSC relies on the photochromic property of WO<sub>3</sub>, i.e., formation of hydrogen tungsten bronze according to the following reaction [4]:

$$WO_3 + x H^+ + x e^- \rightarrow H_x WO_3$$
 (1)

This property has been widely used in many applications such as displays and smart windows [34, 35]. The high conductivity and the related high electromobility of H<sub>x</sub>WO<sub>3</sub> (10 - 20 cm<sup>2</sup> V<sup>-1</sup> s<sup>-1</sup>) allow for efficient electron storage [1].

The SSC consists of a dye-sensitized WO<sub>3</sub> photoelectrode (PE), a positive Platinum (Pt) counter electrode (CE), and a vanadium electrolyte  $(0.01V^{4+} \text{ in } 0.1\text{M H}_2\text{SO}_4, \text{pH} = 1)$ . The working principle is illustrated in **Fig. 1**. Under light illumination (Light Mode), dye molecules (N-719) at their ground state also known as the highest occupied molecular orbital (HOMO, 1.25 V vs NHE)

are first excited by solar irradiance to a higher energy state also known as the lowest unoccupied molecule orbital (LUMO, -1.12 V vs NHE), illustrated by process (b) in Fig. 1a. Upon excitation, electrons are injected in the conduction band of WO<sub>3</sub> (CB, 0.2 V vs NHE) presented by process (c) [19]. Part of the electrons that are injected into the CB of WO<sub>3</sub> will be stored in-situ according to Eq. (1) and process (d), while the rest will contribute to the generated photocurrent (e). To continue the reaction, an electron is injected from the vanadium redox represented by process (a) into the valence band of N-719 to replace the excited electron, which is dictated by the following reaction (f) (VO<sup>2+</sup> + H<sub>2</sub>O  $\rightarrow$  e<sup>-</sup> + 2H<sup>+</sup> + VO<sub>2</sub><sup>+</sup>) [19]. At the Pt CE (positive electrode), VO<sub>2</sub><sup>+</sup> is reduced to VO<sup>2+</sup> (g). In Fig. 1b, under Dark Mode or low light intensity decomposition of H<sub>x</sub>WO<sub>3</sub> (discharge reaction), continues the electric current (h) that remains in the same direction as the photocurrent, while reduction of VO<sub>2</sub><sup>+</sup> occurs at the positive electrode to complete the reaction.

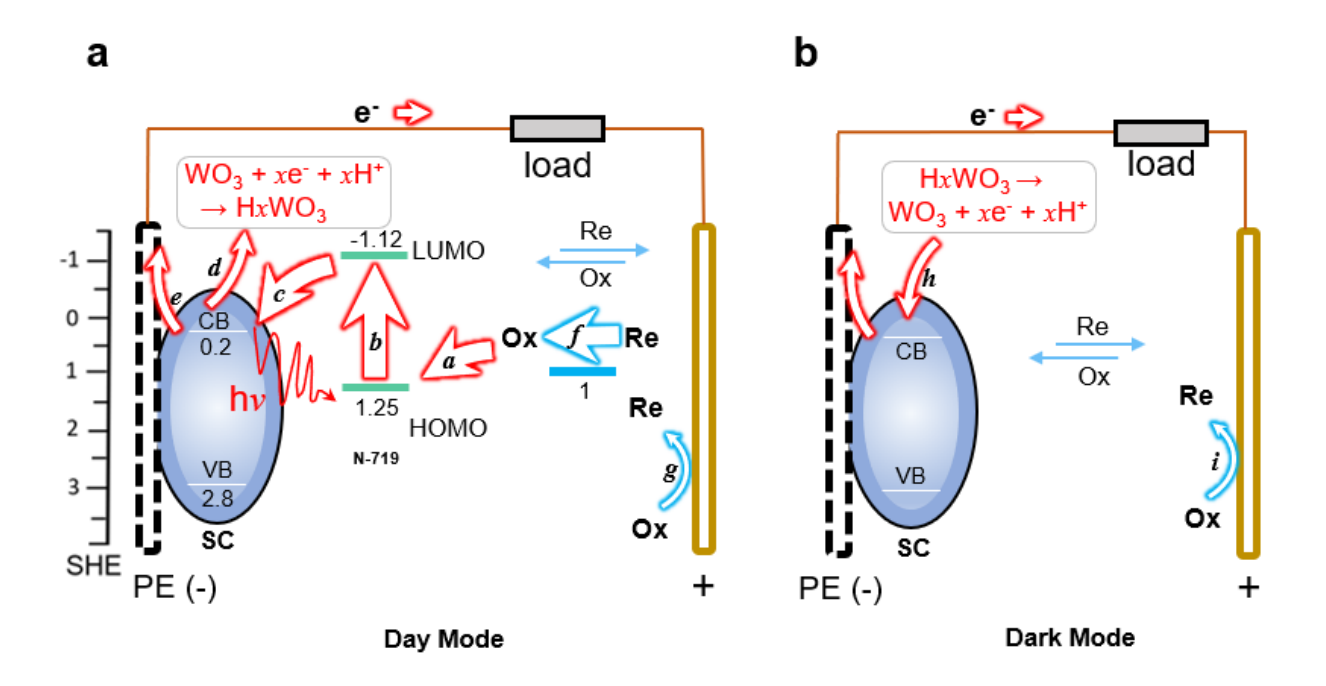


**Fig. 1:** Working Principle of the storage SC under (a) Light Mode and (b) Dark Mode. The unit on the LHS scale is V.

#### 3. EXPERIMENTAL

## 3.1 Fabrication of WO<sub>3</sub> photoelectrode

Three different batches of WO<sub>3</sub> with different particle sizes, i.e., #1 (23-65 nm) from US-Nano, #2 (60-95 nm) from US-Nano, and #3 (~100 nm) from (Sigma-Aldrich), were tested. WO<sub>3</sub> pastes were prepared by mixing WO<sub>3</sub> with alpha-terpineol (Fisher Chemical) in a weight ratio of ca. 1: 1.5. The mixture was stirred at 80 °C and 800 rpm for 60 min until a slick paste was obtained. The resulting paste was then coated on a precleaned FTO glass using a doctor blade and dried at 120 °C for 30 min as described elsewhere [36]. This was followed by high-temperature sintering at 450 °C for 30 min to remove any organic residues. A Titanium chloride (TiCl<sub>4</sub>, Sigma Aldrich) solution in 50 mM was spin-coated on the obtained WO<sub>3</sub>-coated FTO using a spin coater (Laurell Technologies, WS-400BZ-6NPP/LITE) at 3000 rpm for 20s [1, 37], followed by calcination at 450 °C for 30 min. N-719 dye (Sigma Aldrich) adsorption was conducted by immersing the electrode overnight at room temperature in ethanol solution containing 0.3 mM N-719 [19, 37, 38]. Shortly after the film was removed from the N-719 dye solution, 0.05 ml Nafion solution (EW 1100, Sigma-Aldrich) was sprayed on the WO<sub>3</sub> film using an air-brush (TCP global). The Nafion thin layer will assist in immobilizing the dye molecules to reduce dissolution upon extended photoelectrochemical testing.

#### 3.2 Photoelectrochemical measurements

Cyclic voltammetry measurements (CV) were conducted using a VersaSTAT3 potentionstat (Princeton Applied Research) in a three-electrode cell consisting of the dye-sensitized WO<sub>3</sub> working electrode (WE), a platinum counter electrode (CE) and an Ag/AgCl reference electrode (RE) [39]. The electrolyte was 0.01 M vanadium sulfate oxide hydrates (VOSO<sub>4</sub>•xH<sub>2</sub>O, Alfa Aesar, 99.9%) dissolved in 0.1 M H<sub>2</sub>SO<sub>4</sub>. Electrochemical characteristics of the electrolyte were

studied using cyclic voltammetry in an electrochemical cell consisting of a glassy carbon -WE and 20 ml of vanadium electrolyte (pH = 1) at variable scanning rates from 10 mV/s to 500 mV/s. A solar simulator (Newport, USA, equipped with an AM1.5 global filter) positioned at a 1.5-in distance from the photoanode was used to provide solar irradiance for the PEC testing. Zero resistance ammeter (ZRA) function was used for photo-charge/discharge analysis. Linear sweep voltammetry was employed for current-voltage (IV) analysis [36].

### 3.3 Conductivity Measurement

The electrical conductivity of the photoelectrodes was analyzed by the widely used 4-probe measurement. WO<sub>3</sub> (60-95 nm) film was coated on a non-conductive glass substrate using a similar procedure as stated earlier [36, 39]. Four Cu probes were positioned 2 mm apart. A DC current was allowed to pass through the outer probes and the induced voltage in the inner probes was used to evaluate the conductivity (S/m) of the electrode with other inputs including the distance between probes (d), thickness, and film area.

#### 3.4 SEM Characterization.

Prior to SEM surface and cross-section imaging, a vacuum sputter coater (Denton Vacuum Desk IV) was used to deposit a gold (Au) coating on the surface of the WO<sub>3</sub> electrodes [11]. Surface and cross-section images of the WO<sub>3</sub> films were obtained at variable magnifications using Field-emission Scanning Electron Microscope (JEOL JSM-1401F FE-SEM).

## 3.5 Numerical Electrode Microstructure Reconstruction and Transport Study

The previously developed stochastic reconstruction algorithm [40, 41] was adopted herein to create electrode structures and study the random stacking and mixing of WO<sub>3</sub> in an electrode as well their implication to the solid-state electronically conducting path.

#### 4. RESULTS AND DISCUSSION

## 4.1 SEM Images of Photoelectrodes

To understand the impact of WO<sub>3</sub> photoelectrode morphology, including porosity and particle connectedness, on both the photocurrent and storage performance of the SSC, cross-sectional and surface SEM images of three different photoelectrodes were taken. Although a similar photoelectrode fabrication procedure and similar WO<sub>3</sub> loading were used, cross-sectional SEM images demonstrated different WO<sub>3</sub> film thicknesses (Fig. 2 a-c). Estimated from their crosssections, the thickness of three WO<sub>3</sub> electrodes ranges between ~20 and 50 μm. Note that these WO<sub>3</sub> electrodes are significantly thicker than those reported in the literature (e.g., 500nm in reference [42]) with the objective to improve electron storage capability by photochromic reactions. Besides, #3 WO<sub>3</sub> with the largest particle size (~ 100nm, according to Sigma-Aldrich) forms large aggregates which also form big voids. The impact of these aggregates and voids on electrical conductivity and redox species diffusivity will be discussed later in the work. On the other hand, the WO<sub>3</sub> primary particle size seems to impact the secondary particle (agglomerates) shape. The surface SEM images in Fig. 2 d-f show that both #1 WO<sub>3</sub> (primary particle size: 23-65nm) and #2 WO<sub>3</sub> formed nanoflakes; in contrast, #3 WO<sub>3</sub> (~ 100 nm) exhibits spherical-shaped secondary particles with rough surfaces. In addition, careful examination of the electrode surface has clearly revealed surface conglomeration and mud-cracks. As a result, a significant difference in PEC performance is expected when these WO<sub>3</sub> photoelectrodes are employed in the developed SSC. Particularly, the electrical conductivity and PEC reaction kinetics with implication to photocatalytic properties such as electrons injection/collection efficiencies, recombination rates and diffusion coefficient [24] are directly related to the physical and chemical properties such as porosity and electroconductivity of the photoelectrodes.

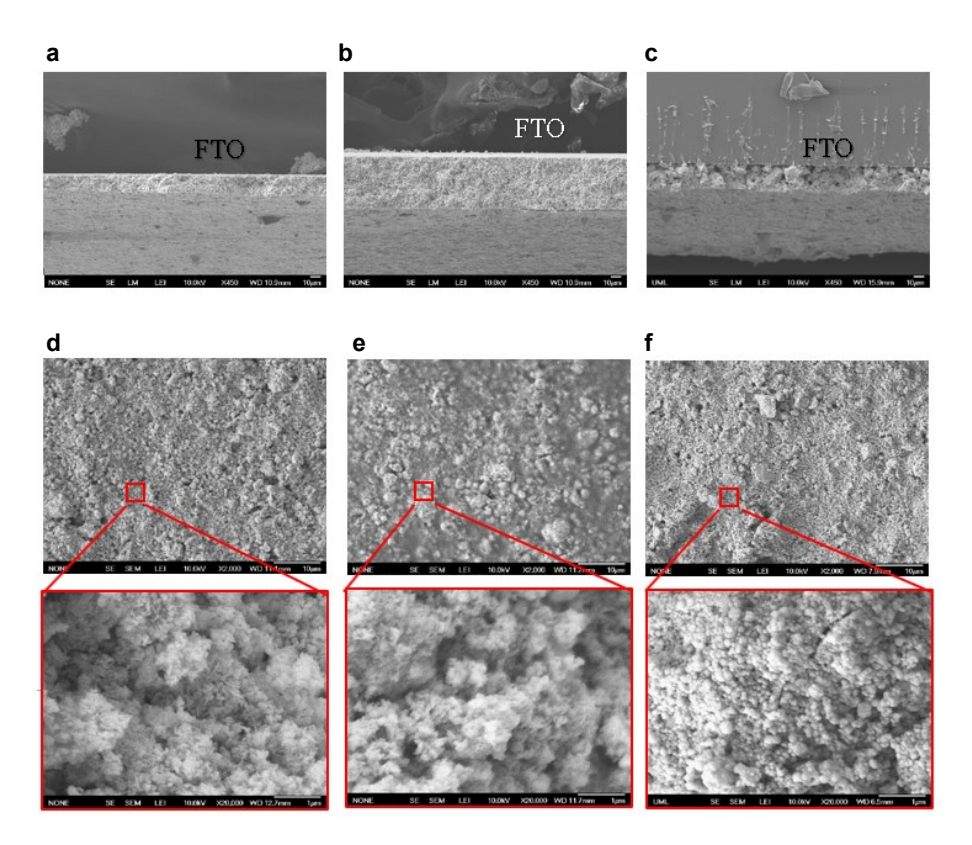


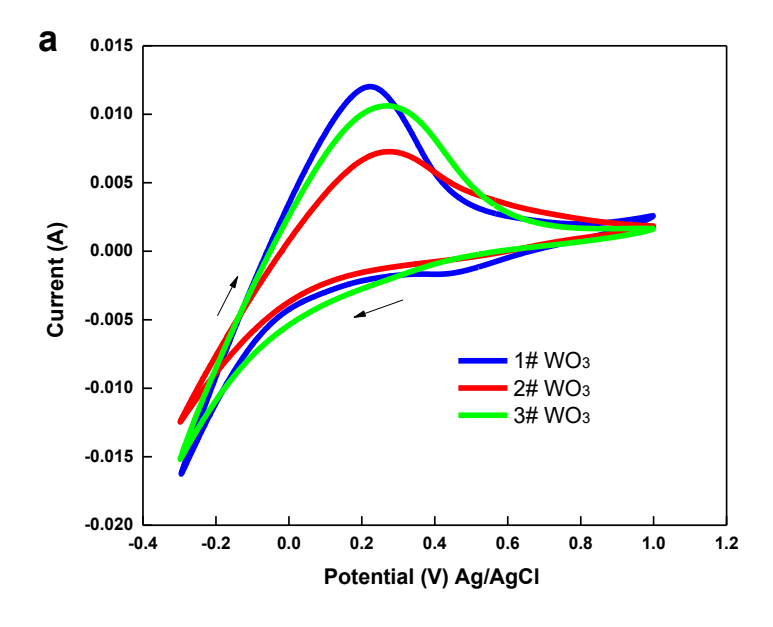
**Fig. 2.** (a-c) Cross-sectional SEM images of WO<sub>3</sub> photoelectrodes fabricated with different: (a) #1 WO<sub>3</sub>, (b) #2 WO<sub>3</sub>, and (c) #3 WO<sub>3</sub>; (d-f) Surface SEM images at different magnifications: (d) #1 WO<sub>3</sub>, (e) #2 WO<sub>3</sub>, and (f) #3 WO<sub>3</sub>.

# 4.2 Electrochemical Characteristics of Vanadium Redox and WO<sub>3</sub>

Electrochemical behavior of different WO<sub>3</sub> photoelectrodes (without dye loading) and VO<sup>2+</sup> was studied using a three-electrode electrochemical cell. The cyclic voltammograms of the WO<sub>3</sub> films, depicted in **Fig. 3**, were obtained by sweeping the potential in the range of -0.3 to +1.0 V vs. Ag/AgCl in 0.1M H<sub>2</sub>SO<sub>4</sub>. The highest oxidation peak current ( $I_a = 13$  mA, corresponding to the reverse reaction of Eq. 1 as well as depicted in process h of **Fig. 1**b) was achieved for 1# WO<sub>3</sub> at the anodic potential of  $E_a = 0.2$  V vs Ag/AgCl. Similarly, #3 WO<sub>3</sub> has an oxidation peak of  $I_a = 10$  mA at a slightly higher oxidation potential  $E_a = 0.25$  V. In contrast, #2 WO<sub>3</sub> has the least anodic peak current, i.e.,  $I_a = 7$  mA. On the other hand, the reduction peaks overlap with hydrogen

adsorption and cannot be clearly identified. In addition, from this figure one can observe a slight increase of the cathodic current (corresponding to the storage current as illustrated in process d of Fig. 1a) for #1 and #3 WO<sub>3</sub> in comparison to #2.

Cyclic voltammograms of  $VO^{2+}$  electrolyte (0.01 M in 0.1M H<sub>2</sub>SO<sub>4</sub>) was obtained in a threeelectrode cell equipped with a glassy carbon as the WE, Pt mesh as the CE, and Ag/AgCl RE at variable scanning rates ranging from 0.01-0.1 V/s. Four redox peaks are observed in **Fig. 3**b: I and III are the reduction peaks of  $VO^{2+}$  ( $V^{4+}$ ) and  $VO_{2^+}$  ( $V^{5+}$ ), and II and IV are the oxidation peaks of  $V^{3+}$  and  $VO^{2+}$  ( $V^{4+}$ ), respectively. Higher scanning rates, though creating higher peak currents, result in electrochemical irreversibility, which is manifested by further separation of oxidation/reduction peak potentials.



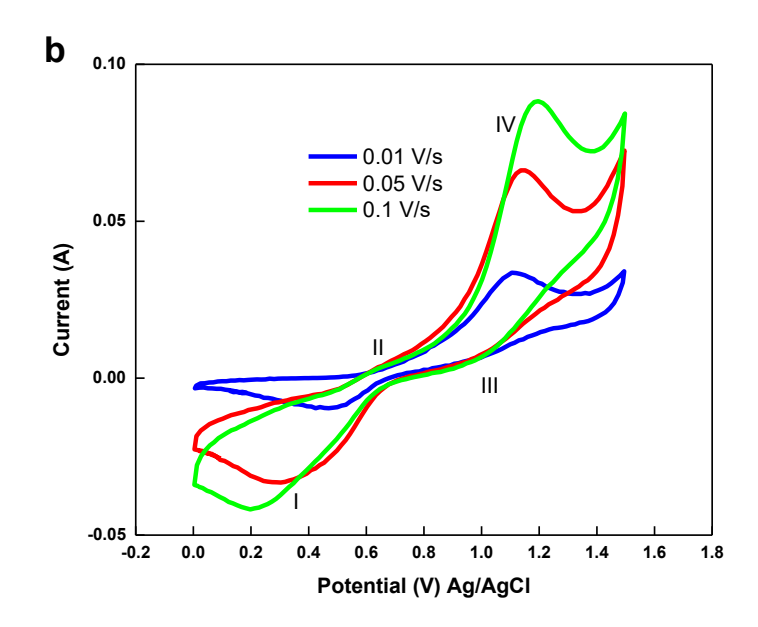


**Fig. 3**: Cyclic voltammograms of (a) WO<sub>3</sub> electrodes made of three different sources: #1 WO<sub>3</sub> (23-65 nm), #2 WO<sub>3</sub> (60-95 nm), #3 WO<sub>3</sub> (~100 nm), and (**b**) 0.01 M VO<sup>2+</sup> electrolyte in 0.1M H<sub>2</sub>SO<sub>4</sub> with scanning rate 0.01-0.1 V/s.

## 4.3 Photocharging and Discharging Studies

To demonstrate the capability of the SSC, ZRA function was used for photo-charge/discharge analysis under both Light Mode and Dark Mode. As has been detailed in reference [9], the SSC has a two-electrode configuration, i.e., a dye-loaded WO<sub>3</sub> photoelectrode and a Pt CE immersed in 0.01 M VO<sup>2+</sup> electrolyte. **Fig. 4** shows the cell photoresponse in alternate Light and Dark modes. In Light Mode, photons excite N-719 dye molecules to generate electrons. The excited electrons are then injected to the WO<sub>3</sub> CB and are further collected in the back of the FTO substrate, contributing to the observed photocurrent. During the 1<sup>st</sup> illumination period in **Fig. 4**, the photoelectrode with #3 WO<sub>3</sub> generates the highest average photocurrent density, i.e., J = 0.2 mA.cm<sup>-2</sup>, which declines but stabilizes in the 2<sup>nd</sup> and 3<sup>rd</sup> illumination periods. This fast decay of photocurrents, which is commonly observed in PEC processes [43], is assigned to the trapping of

photo-generated carriers in traps states, but more likely to the depleted vanadium redox that could not be effectively replenished [44]. On the other hand, #2 WO<sub>3</sub> shows a similar photocurrent as #1 WO<sub>3</sub> in the 1<sup>st</sup> illumination period, but its photocurrent quickly deteriorates in the 2<sup>nd</sup> and 3<sup>rd</sup> illumination periods. This is accompanied by much more appreciable dark current (at least 5-fold higher) than #1 WO<sub>3</sub> as a result of the stored electrons (reaction 1) under illumination. Upon switching to Dark Mode, a sudden decline in photocurrent is noted but both 2# and 3# WO<sub>3</sub> continue to produce current at J<sub>dark</sub> = 0.05 mA.cm<sup>-2</sup> for 100 s until the light was switched on in the next cycle. This observation coincides strongly with our previous results in all-vanadium PEC cells [4, 18], which indicate that when the photogenerated electrons, apart from recombining with holes, have a higher tendency to react with WO<sub>3</sub> along with H<sup>+</sup> ions to form H<sub>x</sub>WO<sub>3</sub>, a more inferior photocurrent is produced.

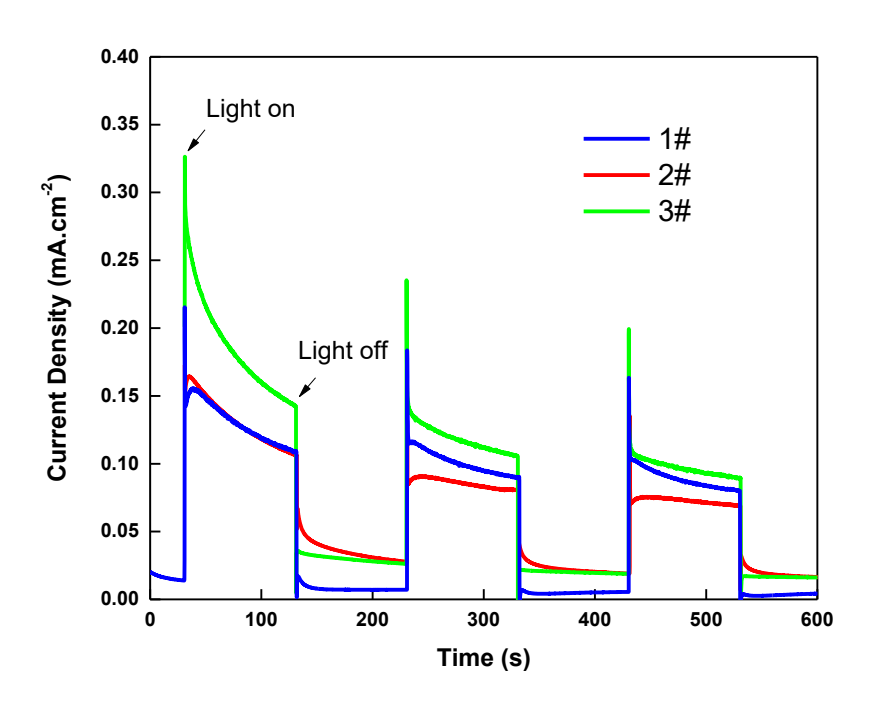


Fig. 4: Photocurrent in alternate light mode and dark mode for different WO<sub>3</sub> photoelectrodes.

## 4.4 Current-Voltage characteristics

To further demonstrate the performance of the developed SSC, current-voltage (IV) characteristics were studied under both Light and Dark modes. In Fig. 5a, three electrodes show similar opencircuit voltages (V<sub>oc</sub>) ranging from 0.43 to 0.48 V. These values are slightly lower than the reported value using iodine electrolyte and TiO<sub>2</sub>/WO<sub>3</sub>, e.g., V<sub>oc</sub> = 0.6V in [33]. The cell with 3# WO<sub>3</sub> demonstrates superior IV performance with a short-circuit current density  $(J_{sc}) \sim 0.5$  mA.cm<sup>-2</sup>, which is twice as much as that of #1 and #2 WO<sub>3</sub> electrodes. The high photocurrent generated in #3 electrode may be directly linked to its large WO<sub>3</sub> particles in the electrode structure (SEM image in Fig. 2c) that result in relatively a high porosity, and therefore higher ion diffusion coefficient and electrical conductivity. However, the Light-Mode IV curves of the SSCs are not correlated to the Dark-Mode performance because of different electron-generating mechanisms. In Fig. 5b, the three cells, after a short-period illumination (< 5 min), show comparable Dark-Mode cell Voc to those under illumination (Fig. 5a) but inferior Jsc which is solely generated from the stored charged. Overall, the transient IV characteristics in Fig. 5 seem to be in a good agreement with the ZRA results in Fig. 4 for both #2 and #3 electrodes. For #1 WO<sub>3</sub> electrode, the high J<sub>sc</sub> under darkness could not be sustained due to its high internal series resistance, manifested by its rapid current drop with increasing voltage, which also contributes to the observed poor dark current in Fig. 4 and electrochemical oxidation current in Fig. 3b.

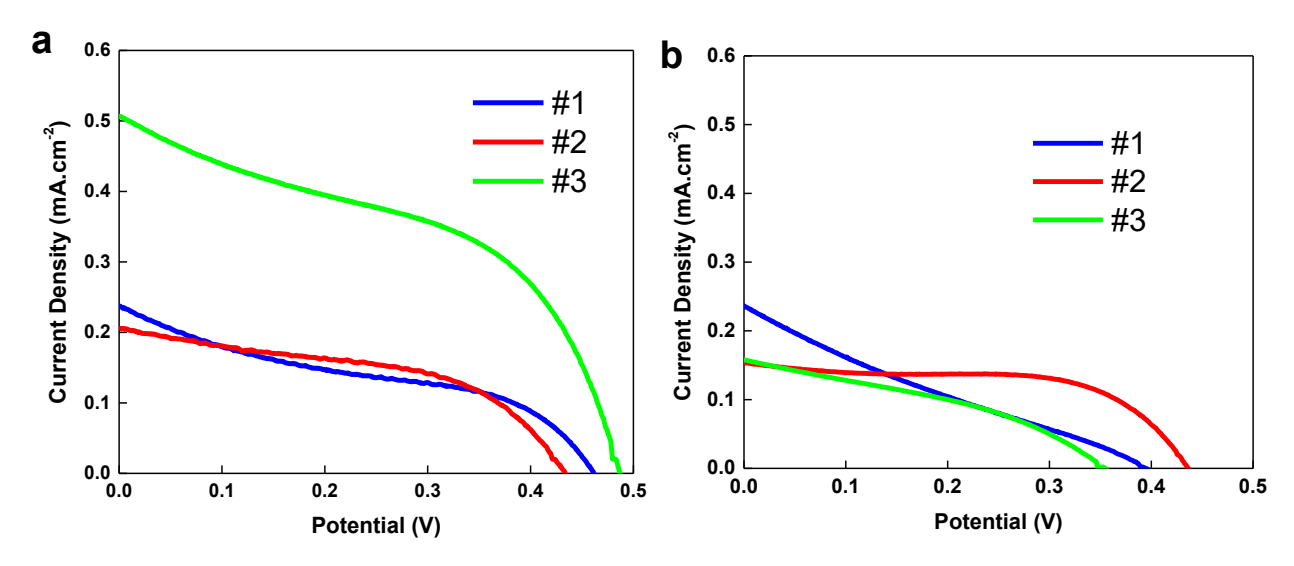
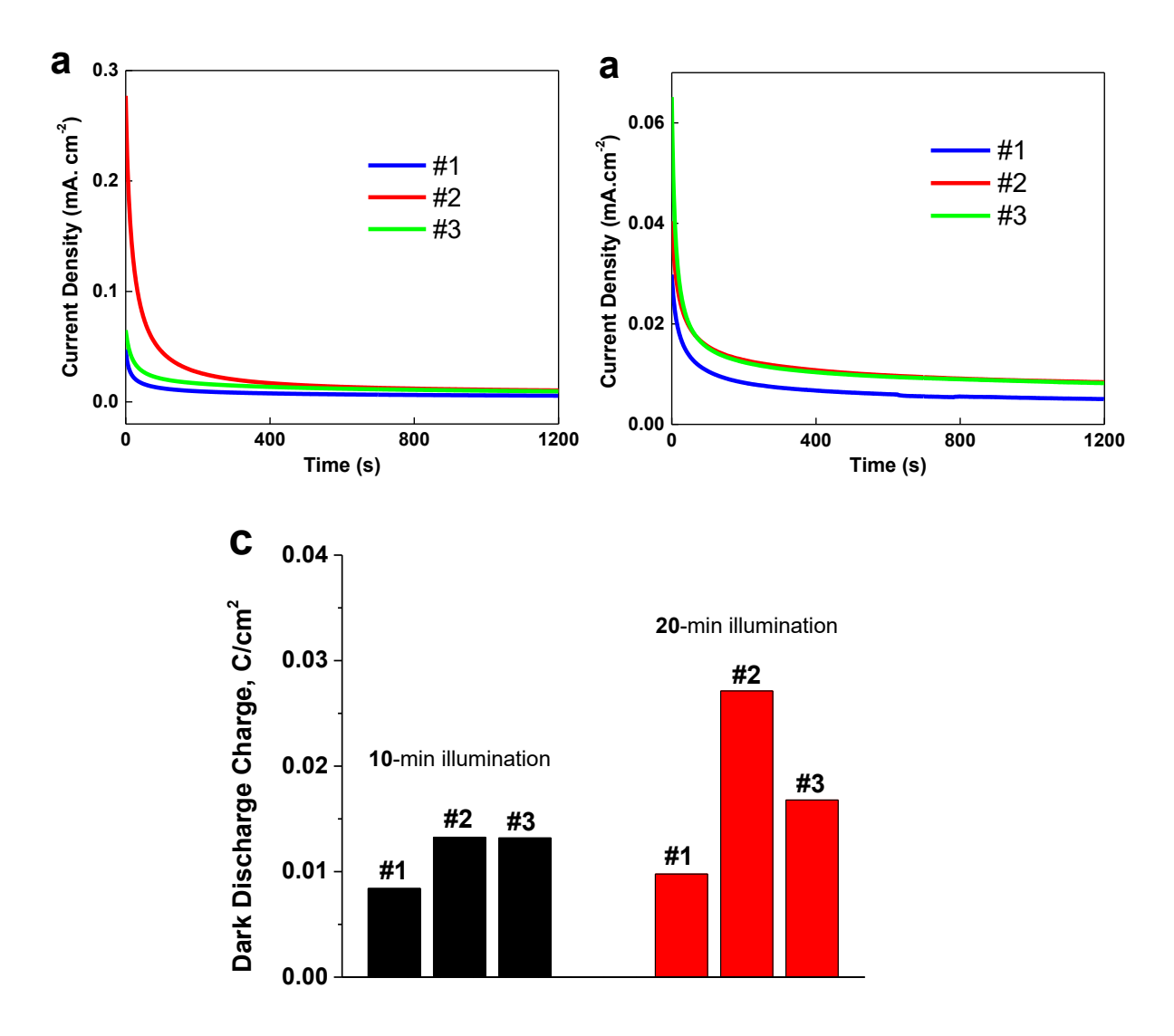


Fig. 5: Transient IV-characteristics for different SSCs (a) under illumination (b) under dark.

## 4.5 Long-term Photocharging/Discharging Measurement

To evaluate the long-term Dark-Mode discharging performance, the cells were first photo-charged for either 20 min or 10 min before being discharged under darkness for over 20 min using the ZRA function. **Fig. 6**a displays the dark currents for the three electrodes recorded after a 10-min photocharge. #2 WO<sub>3</sub> electrode initially achieved a discharge current density of J<sub>dark</sub> = 0.28 mA.cm<sup>-2</sup> which gradually declined to J<sub>dark</sub> = 0.02 mA.cm<sup>-2</sup> after 20-min discharge. The observed much thicker #2 electrode (twice as much as the other two, as revealed in the SEM images in **Fig. 2b**) may have contributed to its higher electron storage capacity. On the other hand, #1 WO<sub>3</sub> and #3 WO<sub>3</sub> only reach the initial discharge current densities of 0.07 mA. cm<sup>-2</sup> and 0.05 mA.cm<sup>-2</sup>, respectively. For the 10-min photocharging test in **Fig. 6b**, both #3 and #2 WO<sub>3</sub> electrodes show higher dark current densities (which are much smaller than those with 20-min light illumination in **Fig. 6a**), with respectively initial values at 0.07 mA and 0.04 mA, than #1 electrode.



**Fig. 6**. Dark-condition discharge performance: (a) transient discharge current with 20-min illumination, (b) transient discharge current with 10-min illumination, and (c) integrated charges during the dark-condition discharge for the three electrodes.

The electron storage capacity of the electrodes is assessed by the total released charge during the dark-mode discharging period [45] and is plotted in **Fig. 6**c. Extending the photocharging period from 10 min to 20 min, the electron storage capacity of #2 electrode doubles, increasing from 0.013 to 0.027 C/cm<sup>2</sup>. Again, the thicker #2 electrode (50 µm) as previously seen in the SEM images in **Fig. 2**b can be correlated to its larger charge storage capacity. In contrast, #1 and #3

electrodes only show a slight improvement in storage capacity, at 16% and 27%, respectively, when the photocharging duration doubled. This suggests that their full storage capacity has been reached even under 10-min light illumination. The above results collectively demonstrate the importance of extending photoelectrode thickness to improve storage capacity.

#### 4.6 Photoanode numerical Simulation

So far, the results from the SEM images and photo-/electrochemical studies have pointed to the electrode microstructure as the key performance-limiting factors of the SSC. The photoelectrode microstructure including porosity and particle connectedness has a significant implication on ion diffusion, solid-state electrical transport, and therefore the photocurrent and storage capacity. However, the SEM images in Fig. 2 could not provide insightful information regarding the connectedness of secondary WO<sub>3</sub> particles and the voids formed between them as they would impact both electronic conductivity and ionic transport of vanadium ions. Instead, we turn to numerical analysis to systematically quantify electrode microstructure and understand its impact on the observed photoelectrochemical characteristics. For the above reason, the previously developed stochastic microstructure reconstruction algorithm [40, 41] based on the principle of nucleation and growth was adopted herein to gain in-depth insights. Fig. 7 shows representative stochastically-reconstructed microstructures for the three electrodes with inputs from the SEM images. To create statistically enriched microstructure representations, the stochastic reconstruction model generates five 3D realizations for each electrode with the same inputs, i.e., the reconstruction seed number and porosity. The former, adopted as a statistical descriptor, is estimated from the SEM images, e.g., shape, agglomerates, and size and distribution pertinent to the microstructural property of the electrodes. The latter was calculated using electrode properties such as cross-section thickness, WO<sub>3</sub> loading, and WO<sub>3</sub> density. A reconstructed microstructure

size consisting of more than 20~50 primary WO<sub>3</sub> particles (corresponding to particle size ranging from 20 to 100 nm) as shown in Fig. 7 should be sufficient to achieve realistically representative electrode properties, assuming there are no major structural defects. Furthermore, the reconstructed structure has been verified to be consistent with electron-micrographic observations [40, 41]; therefore, particle connectivity, constituent interfaces, and distribution can be directly accessed and systematically studied from the reconstructed microstructure. Fig. 7 shows that both porosity and reconstruction seed number have a significant impact on electrode microstructure. Comparison between Fig. 7a and 7c indicate that at similar porosity levels a doubled seed # results in slightly improved dispersion of the secondary WO<sub>3</sub> particles. Though the primary particle size of WO<sub>3</sub> is between 200-100 nm, its agglomeration leads to size of 300-500 nm or even bigger as shown in Fig. 7. When both porosity and seed # double as seen in Fig. 7b in comparison to Fig. 7c, a noticeable reduction in WO<sub>3</sub> agglomeration and particle discontinuity (or necks) appears. These necks act as electron transport barriers and will contribute to conductivity loss.

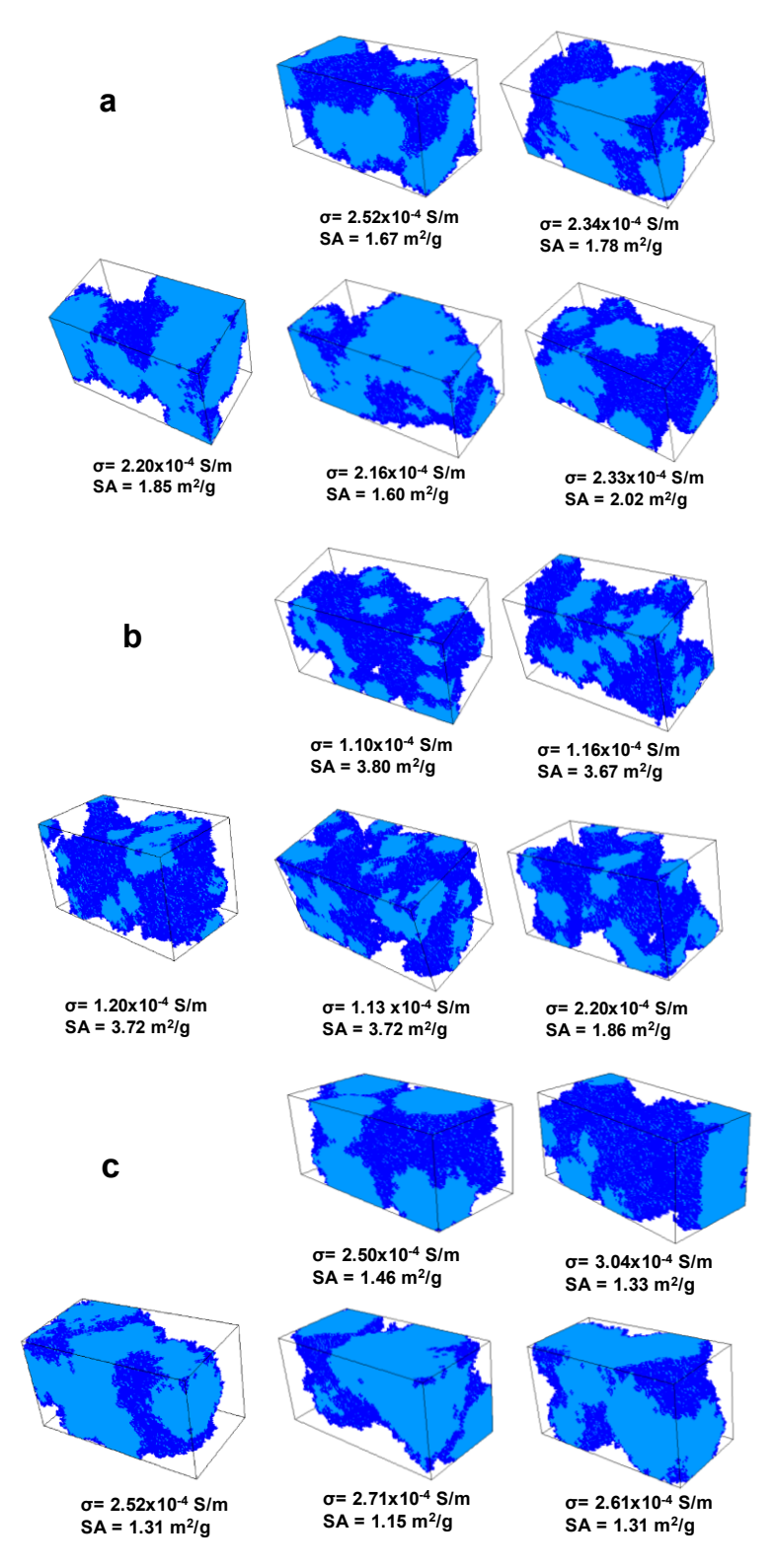


**Fig. 7.** The numerically reconstructed WO<sub>3</sub> electrodes: (a) #1 (Seed# = 30, Porosity = 28%), (b) #2 (Seed# = 50, Porosity = 47%), and (c) #3 (Seed# = 15, Porosity = 26%). The reconstructed size is  $600 \text{ nm} \times 300 \text{ nm} \times 300 \text{ nm}$ .

Table 1. Photoelectrode properties and their photoelectrochemical performance

Sample #	Effective Conductivity (S/m)	SA (m²/g)	Effective Diffusivity (m²/s)*	Photo- current, (mA/cm²)**	Storage capacity, (C/cm²)***
#1 (Seed# = 30, ε = 28%)	2.31 x 10 <sup>-4</sup>	1.78	2.03 x 10 <sup>-9</sup>	0.088	0.010
#2 (Seed# = 50, ε = 47%)	1.12 x 10 <sup>-4</sup>	3.70	3.04 x 10 <sup>-9</sup>	0.073	0.027
#3 (Seed# = 15, ε = 26%)	2.64 x 10 <sup>-4</sup>	1.32	1.25 x 10 <sup>-9</sup>	0.097	0.017

<sup>\*</sup> Estimated using  $D_e = D_0 \cdot (\frac{\varepsilon - X_0}{1 - X_0})^2$ , where  $D_0$ ,  $\varepsilon$ , and  $x_0$  are intrinsic conductivity, photoelectrode porosity, and percolation critical value, respectively.  $x_0$  was assigned an arbitrary value of 0.1.

## 4.7 Analysis of Photoelectrochemical Transport Process

The reconstructed structures not only provide important localized information at the pore level, but also can be translated into a structure-level transport property such as effective electrical conductivity. The effective electrical conductivity was first evaluated (labeled in **Fig. 7** also listed in **Table 1**) from the reconstructed structures because they capture the collective information of localized transport, tortuosity and connectedness of the electrode materials. Fixed electrical potentials were applied at the left and right boundaries, e.g., 0 and 1V, respectively. The electrical current and thus the conductivity under this potential gradient was determined by running a full 3D simulation. **Table 1** also shows the electrical conductivity value of #2 WO<sub>3</sub> electrode that was experimentally measured using the four-probe method. In addition, the surface of the WO<sub>3</sub> that is exposed to the liquid electrolyte can be directly assessed from the reconstructed structure and is adopted as the electrochemical active area (listed in **Table 1**).

<sup>\*\*</sup> Taken as the averaged photocurrents from the 2nd cycle in Fig. 4.

<sup>\*\*\*</sup> From Fig. 6, after 20-min illumination.

<sup>\*\*\*\*</sup> Experimentally evaluated conductivity of #2 electrode: 3.08 x 10<sup>-4</sup> S/m.

Results in **Table 1** show that a higher electrode porosity results in a larger specific active area (SA, m²/g) but lower connectivity. Conductivity clearly shows an increasing trend with the reconstruction seed number at similar porosity levels. Moreover, though the experimentally measured conductivity value for the #2 WO<sub>3</sub> was found to be larger than those evaluated from the reconstructed microstructures, which is a possibility due to unexpected electrode compression during the measurement; however, the comparison between the experimental and simulated values suggests a good agreement. This agreement was also observed for reconstructed Li-ion battery electrodes [40].

Species transport in the electrodes also depends on the microstructure, as demonstrated in **Table 1** where VO<sup>2+</sup> diffusivity was calculated for different photoelectrodes. The general trend is that larger porosity values result in voids in the photoelectrode that are available for redox transport, and therefore an increase in transport resistance. This effect is so significant that it could even overweight the impact of larger seed numbers on species diffusivity that may cause pore disconnectedness. As one can see, the VO<sup>2+</sup> diffusion coefficient in #2 WO<sub>3</sub> is about 43% and 150% higher than those for #1 and #3 electrodes, respectively, primarily because of the doubled porosity value even with its larger seed number (therefore better WO<sub>3</sub> dispersion).

Furthermore, a comparison of photoelectrode characteristics and the photoelectrochemical performance could help to identify key parameters in determining both photocurrent and storage capacity (illustrated in **Fig. 1, 2**). In this study, we intentionally employed thick (up to ~ 50μm) WO<sub>3</sub> electrodes for the purpose of achieving appreciable electron storage capacity and these electrodes also lead to a high level of dye loading. Therefore, judging from the test results in **Table 1**, it is safe to conclude that under the cell configuration in this study the specific active area (SA), and therefore the photogeneration rate of electrons, don't seem to be a limiting factor of PEC

performance. Similarly, the effective diffusivity of redox in the electrolyte is not expected to be a dominating factor in PEC performance. On the other hand, both the photocurrent and electrode storage capacity seems well correlated to the effective electrical conductivity. The lattice of WO<sub>3</sub> is capable of accommodating considerable ion/electron insertion. However, upon the intercalation, the structure of WO<sub>3</sub> is known to deform and the resultant structural deformation could lead to significant impedance to electrical transport. Therefore, the effective electrical conductivity seems to be a tunable parameter that can be used to control both the photocurrent and storage capacity. As seen in Fig. 1, the electrons that contribute to the experimentally observed photocurrents need to travel through a long 3D interconnected network of WO<sub>3</sub> particles to the backside of the electrode, as opposed to those that are stored locally according to reaction 1. This indicates that a high electrical conductivity, which could be realized by a thin but compact photoelectrode (e.g., #3), could facilitate the long-distance electron travel, thus favoring the photocurrent rather than the storage. Alternatively, a thick electrode with a large porosity value (i.e., #2 electrode) restricts the photogenerated electrons to localized storage reactions. This increases the storage capacity but may also slow down the Dark-Mode discharge reaction, as evidenced by the relatively smaller J<sub>sc</sub> for #2 electrode in **Fig. 5**b.

#### **CONCLUSION**

In this work, an integrated solar storage cell was studied in terms of PEC performance and storage capacity with different photoelectrodes fabricated using three different batches of WO<sub>3</sub> nanoparticles. Experimental and simulation results collectively exhibited that the photoelectrode microstructure including the porosity and particle connectedness has a significant implication to ion diffusion, solid-state electrical transport, and therefore the photocurrent and storage capacity. The electron storage capacity of the electrodes, assessed by the total released charge during the

dark-mode discharging period, is found to be determined by the photoelectrode thickness. The electrical conductivity has been identified as a key factor to control the balance between the photocurrent and storage current. Though in the present system, the dark current is noticeably inferior to the photocurrent as a result of sluggish electrochemical kinetics of WO<sub>3</sub> discharge reactions, this work provides a promising approach and may serve as a model to be extended to other systems with new chemistries and fast electrochemical kinetics that could possibly establish a reliable yet affordable integrated solar storage cells.

#### **ACKNOWLEDGMENT**

This work was supported by Massachusetts Clean Energy Center (Award # S53000000036086). It is also partially supported by the National Science Foundation under Grant Number ECCS-1739137 and IIP- 1918979. H.A. and F.L also acknowledge the constructive comments received at the Energy Materials Conference 2018, Newton, MA, Aug. 27-28 when the paper reporting this work was presented.

### **REFERENCES**

- [1] W. Zhao, X.-F. Wang, E. Zheng, Y. Wei, Y. Sanehira, G. Chen, Journal of Power Sources, 350 (2017) 28-34.
- [2] S. Licht, G. Hodes, R. Tenne, J. Manassen, Nature, 326 (1987) 863-864.
- [3] Z. Wei, D. Liu, C. Hsu, F. Liu, Electrochemistry Communications, 45 (2014) 79-82.
- [4] D. Liu, W. Zi, S.D. Sajjad, C. Hsu, Y. Shen, M. Wei, F. Liu, Acs Catalysis, 5 (2015) 2632-2639.
- [5] Y. Shen, Z. Wei, D. Liu, F. Liu, ECS Transactions, 72 (2016) 179-185.
- [6] Z. Wei, Y. Shen, D. Liu, C. Hsu, S.D. Sajjad, K. Rajeshwar, F. Liu, Nano Energy, 26 (2016) 200-207.
- [7] Z. Wei, Y. Shen, D. Liu, F. Liu, Meeting Abstracts, MA2016-01 (2016) 198.
- [8] Z. Wei, N.A. Siddique, D. Liu, S. Sakri, F. Liu, Advances in Energy Research, 4 (2016) 285-297.
- [9] Y. Shen, Z. Wei, D. Liu, H. Almakrami, F. Liu, Materials Research Bulletin, 96 (2017) 431-436.
- [10] Z. Wei, H. Almakrami, G. Lin, E. Agar, F. Liu, Electrochimica Acta, (2017).
- [11] D. Liu, F. Liu, J. Liu, Journal of Power Sources, 213 (2012) 78-82.
- [12] D. Liu, F. Liu, ECS Meeting Abstracts, 1201 (2012) 184.
- [13] D. Liu, Z. Wei, Y. Shen, S.D. Sajjad, Y. Hao, F. Liu, Journal of Materials Chemistry A, (2015).
- [14] C. Hsu, Y. Shen, Z. Wei, D. Liu, F. Liu, Journal of Alloys and Compounds, 613 (2014) 117-121.
- [15] Y. Shen, Z. Wei, D. Liu, H. Almakrami, F. Liu, Materials Research Bulletin, (2017).
- [16] Z. Wei, Y. Shen, D. Liu, F. Liu, Sci Rep, 7 (2017) 629.
- [17] D. Liu, F. Liu, J. Liu, Journal of Power Sources, 213 (2012) 78-82.
- [18] D. Liu, Z. Wei, C.-J. Hsu, Y. Shen, F. Liu, Electrochimica Acta, 136 (2014) 435-441.

- [19] N. Prabhu, S. Agilan, N. Muthukumarasamy, T.S. Senthil, Journal of Materials Science: Materials in Electronics, 25 (2014) 5288-5295.
- [20] W. Ghann, T. Chavez-Gil, C.I. Goede, H. Kang, S. Khan, H. Sobhi, F. Nesbitt, J. Uddin, Advances in Materials Physics and Chemistry, 07 (2017) 148-172.
- [21] D. Kuang, J. Brillet, P. Chen, M. Takata, S. Uchida, H. Miura, K. Sumioka, S.M. Zakeeruddin, M. Grätzel, ACS Nano, 2 (2008) 1113-1116.
- [22] A. Yella, H.W. Lee, H.N. Tsao, C. Yi, A.K. Chandiran, M.K. Nazeeruddin, E.W. Diau, C.Y. Yeh, S.M. Zakeeruddin, M. Gratzel, Science, 334 (2011) 629-634.
- [23] S. Mathew, A. Yella, P. Gao, R. Humphry-Baker, B.F. Curchod, N. Ashari-Astani, I. Tavernelli, U. Rothlisberger, M.K. Nazeeruddin, M. Gratzel, Nat Chem, 6 (2014) 242-247.
- [24] A.K. Chandiran, M. Abdi-Jalebi, M.K. Nazeeruddin, M. Grätzel, ACS Nano, 8 (2014) 2261-2268.
- [25] Q. Tang, W. Zhu, B. He, P. Yang, ACS Nano, 11 (2017) 1540-1547.
- [26] S. Buhbut, S. Itzhakov, E. Tauber, M. Shalom, I. Hod, T. Geiger, Y. Garini, D. Oron, A. Zaban, ACS Nano, 4 (2010) 1293-1298.
- [27] M. Freitag, J. Teuscher, Y. Saygili, X. Zhang, F. Giordano, P. Liska, J. Hua, S.M. Zakeeruddin, J.-E. Moser, M. Grätzel, A. Hagfeldt, Nature Photonics, 11 (2017) 372-378.
- [28] N. Bagheri, A. Aghaei, M.Y. Ghotbi, E. Marzbanrad, N. Vlachopoulos, L. Häggman, M. Wang, G. Boschloo, A. Hagfeldt, M. Skunik-Nuckowska, P.J. Kulesza, Electrochimica Acta, 143 (2014) 390-397.
- [29] G. Wee, T. Salim, Y.M. Lam, S.G. Mhaisalkar, M. Srinivasan, Energy & Environmental Science, 4 (2011) 413-416.
- [30] C.-Y. Hsu, H.-W. Chen, K.-M. Lee, C.-W. Hu, K.-C. Ho, Journal of Power Sources, 195 (2010) 6232-6238.
- [31] X. Zhang, X. Huang, C. Li, H. Jiang, Advanced Materials, 25 (2013) 4093-4096.
- [32] M. Skunik-Nuckowska, K. Grzejszczyk, P.J. Kulesza, L. Yang, N. Vlachopoulos, L. Häggman, E. Johansson, A. Hagfeldt, Journal of Power Sources, 234 (2013) 91-99.

- [33] W. Li, G. Jin, H. Hu, J. Li, Y. Yang, Q. Chen, Electrochimica Acta, 153 (2015) 499-507.
- [34] L. Zhang, W. Wang, S. Sun, D. Jiang, Applied Catalysis B: Environmental, 168-169 (2015) 9-13.
- [35] P.P. González-Borrero, F. Sato, A.N. Medina, M.L. Baesso, A.C. Bento, G. Baldissera, C. Persson, G.A. Niklasson, C.G. Granqvist, A. Ferreira da Silva, Applied Physics Letters, 96 (2010) 061909.
- [36] G. Kim, M. Oh, Y. Park, Sci Rep, 6 (2016) 33400.
- [37] J. Li, H. Zhang, W. Wang, Y. Qian, Z. Li, Physica B: Condensed Matter, 500 (2016) 48-52.
- [38] S.-W. Lee, K.-S. Ahn, K. Zhu, N.R. Neale, A.J. Frank, The Journal of Physical Chemistry C, 116 (2012) 21285-21290.
- [39] Y. Liu, J. Li, W. Li, H. He, Y. Yang, Y. Li, Q. Chen, Electrochimica Acta, 210 (2016) 251-260.
- [40] N. Siddique, A. Salehi, F. Liu, Journal of Power Sources, 217 (2012) 437-443.
- [41] N.A. Siddique, F. Liu, Electrochimica Acta, 55 (2010) 5357-5366.
- [42] S. Bogati, A. Georg, W. Graf, Solar Energy Materials and Solar Cells, 163 (2017) 170-177.
- [43] T. He, L. Wang, F. Fabregat-Santiago, G. Liu, Y. Li, C. Wang, R. Guan, Journal of Materials Chemistry A, 5 (2017) 6455-6464.
- [44] Z. Wei, Y. Shen, D. Liu, F. Liu, Scientific Reports, 7 (2017) 629.
- [45] C. Ng, Y.H. Ng, A. Iwase, R. Amal, ACS Applied Materials & Interfaces, 5 (2013) 5269-5275.